Effects of Wing Elasticity on Tip Vortex: 3D Deformation and 2D3C Flow Field Measurements

Qinfeng Guo[1], Jinjun Wang[1,*]

1: Fluid Mechanics Key Laboratory of Education Ministry, Beihang University, China
* Correspondent author: jjwang@buaa.edu.cn

Keywords: Wind tunnel experiment, Elastic wing, 3D deformation, Tip vortex

ABSTRACT

As aircraft embrace broader applications, the flexible wing presents a promising avenue to enhance aircraft performance across a wide range of flight conditions. Although the aerodynamic benefits of wing deformation are widely recognized, the present understanding of the tip vortex is relatively limited. This work experimentally examines the effects of wing deformation on the tip vortex of a simplified aircraft model with two kinds of elastic wings and a rigid wing. The 3D deformations and 2D3C flow fields are measured using a synchronous measurement system, which includes the high accuracy deformation measurement (HADM) method and the stereoscopic particle image velocimetry (SPIV). It is shown that increased wing elasticity leads to greater bending, with the wing tip moving along the streamwise, vertically upward, and spanwise inward directions. These deformations are closely linked to aerodynamic forces and influence the tip vortex positions. The more elastic wing, EW2, exhibits the highest vortex core position, more than 0.5 times the length of the wing root, while the other one, EW1, shows the strongest vortex in the lift-increased regime. In the early wakes, the tip vortex of the elastic wing is elongated along the spanwise direction, resulting in an asymmetric shape. As it convects downstream, the vortex core disperses via viscous diffusion, resulting in a relatively more circular shape with decreased vorticity.

1. Introduction

As aircraft evolves to embrace a wider flight envelop, higher maneuverability, and multiple task adaptability, the demand for enhanced aerodynamic performance becomes more and more significant. The flexible wing, possessing the unique capability to deform and vibrate, presents a promising avenue to enhance aircraft performance across a broad range of flight conditions (Shyy et al., 1999, 2005; Lian et al., 2003).

The flexible wing can be traced back to the Wright Brothers' flyer, where the compliant membrane served as lifting surface and controlled the roll through wrapping (Anderson, 1996). More recently,

Song et al. (2008) proposed a bioinspired, thin membrane to investigate the dependence of aerodynamic performance on membrane compliancy. It was observed that the membrane wings had a higher lift slope, maximum lift coefficients, and a delayed stall compared to the rigid wing. These benefits were consistently confirmed by many other studies on flexible wing as well as its applications in aircraft (Bleischwitz et al, 2017; He & Wang, 2020; Guo et al., 2021; Tiomkin & Raveh 2021).

The mechanism behind the performance improvement of flexible wing is the strong coupling between the vortex and structure. Guo et al. (2023) adopted elastic plates in the fixed-wing aircraft model to passively vibrate with the enhanced inertia and elastic forces. Two elastic wings and one rigid wing were used in the wind tunnel experiments, and the effects of wing elasticity on the aircraft aerodynamic performance were investigated. It was observed that the two elastic wings exhibited different aerodynamic performances, classified as the lift-enhancement wing and the drag-reduction wing, respectively. The lift-enhancement wing is relatively less elastic, which presents a torsional vibration mode and a smaller time-averaged deformation. Similar lift enhancement accompanied by a specific vibration mode was also observed in flexible delta wings (Gursul et al., 2014). For the drag-reduction wing, high elasticity results in large bending and twisting, contributing to the decrease of wake deficit and the reduction of lift-induced drag.

While the aerodynamic characteristics of different elastic wings are recognized, the tip vortex, strongly correlated with wing performance, receives little attention. Wing bending, twisting, as well as vibration could significantly influence the characteristics of the tip vortex, as it forms around wing tips due to pressure differences between the upper and lower surfaces (Anderson, 1996). In this paper, aircraft model with two elastic wings and a rigid wing is adopted to investigate the effects of wing elasticity on the tip vortex characteristics. Wind tunnel experiments, including a synchronous measurement of 3D deformation and 2D3C flow field, are conducted. The correlations between wing deformation and tip vortex characteristics are revealed.

2. Experimental Methods

The experiment is conducted in the low-speed circulation wind tunnel D1 at Beihang University (BUAA). The test section is oval with 1.02 m × 0.76 m inlet and 1.07 m × 0.82 m outlet. The experimental freestream velocity U_∞ is fixed at 40 m/s.

The configuration of the aircraft model is shown in Fig. 1, the same as that in the works of Guo et al. (2023). During the experiment, two kinds of elastic plate wings and a pair of rigid plate wings are alternately installed on the rigid fuselage. The length of wing root is c_{root} = 39.5 mm, and the span of the aircraft model is 269.7 mm. The Reynolds number based on c_{root} is Re = 1.1 × 10^5. Two elastic wings are made of epoxy insulation board (EIB) with elastic modulus E of 24 GPa and polymethyl methacrylate (PMMA) with E = 3 GPa, respectively. The rigid wing is made of aluminum with E = 70 GPa. In this paper, EW1, EW2, and RW are used to mark the less elastic wing, the more elastic one, and the rigid one, respectively. More detailed parameters of the model can refer to the work of Guo et al. (2023).

High accuracy deformation measurement (HADM) method, a kind of structured-light surface imaging technology developed from Fourier transform profilometry (FTP), is used to measure the 3D wing deformation with a camera and a projector (Takeda & Mutoh, 1983; Guo & Wang, 2023). As displayed in Fig. 1, a digital light processing (DLP) projector is utilized to project a sinusoidal fringe pattern with a 15-pixel period, covering an area of 280 mm × 160 mm. A charge coupled device (CCD) camera with a resolution of 2456 × 2058 pixels is used to capture a field of view of approximately 300 × 250 mm, which covers the entire span of the model. The reconstruction algorithm is the same as that in the works of Guo & Wang (2023), which only needs one shot of the deformed wing to obtain a 3D wing surface.

Stereoscopic particle image velocimetry (SPIV) is conducted to measure the 2D3C flow fields. An Nd:YAG double pulsed laser with power of 500 mJ and wavelength of 532 nm is employed as light source. Two CCD cameras with a tailored resolution of 1280 × 1280 pixels are used to capture the field of view of about 70 mm × 70 mm. The measured planes are vertical to the freestream and located downstream of the wing tip at distances of x/c_{root} = 0.5, 1, 2, 3, 4, 5. To obtain the velocity fields, the multiple iterative Lucas-Kanade algorithm is used to process the raw images with 75% overlap and final interrogation areas of 32 × 32 pixels, resulting in a spatial resolution of 8 pixels (Champagnat et al., 2011; Pan et al., 2015).
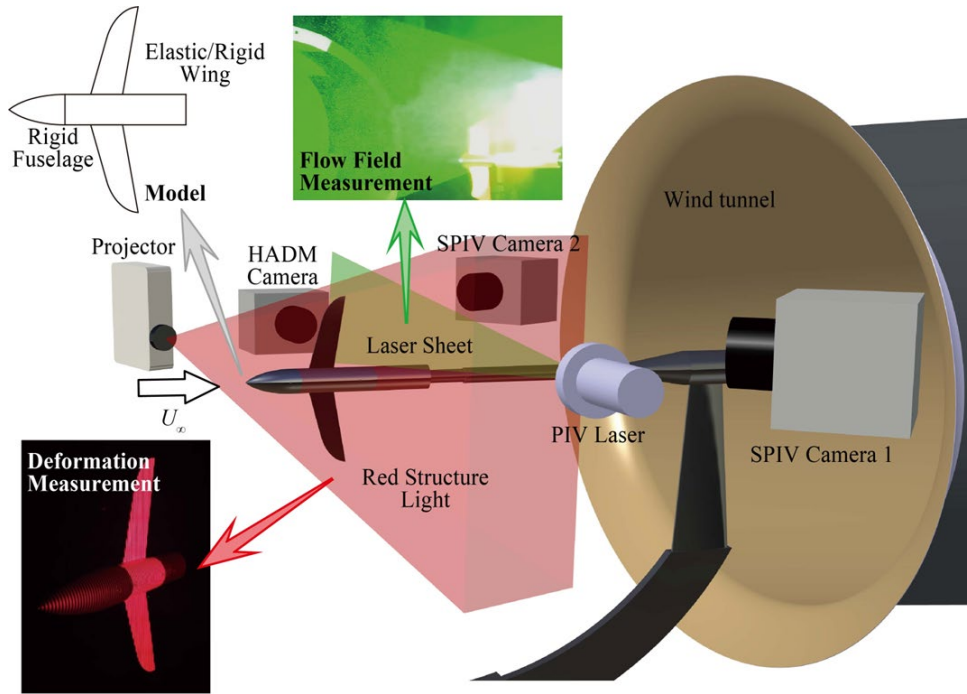
Figure. 1 Schematic sketch of the experimental setup.

To achieve synchronous measurement of deformation and flow field, a precision synchronizer with an accuracy of 0.25 ns is employed to control the system. The projected fringe pattern for deformation measurement is set to red for distinction from the green PIV laser. The camera lens is equipped with a long-pass edge optical filter with a cut-on wavelength of 560 nm to eliminate interference from the PIV laser. Meanwhile, the PIV camera lenses are fitted with bandpass optical filters, featuring a center wavelength of 532 nm and a half-bandwidth of 10 nm. 3000 instantaneous velocity fields and deformations are obtained in a single experiment with a sampling frequency of 4 Hz. The measured angles of attack are AoA = 6°, 12°, and 20°, which represents the linear-increased lift regime, lift-enhancement regime and the post-stall regime according to the works of Guo et al. (2023).

3. Results

3.1 Wing deformation

Figure 2 shows the time-averaged wing shapes at AoA = 12°. The origin of coordinate system is located at the undeformed wing tip. The x, y, and z axes align with the streamwise, vertical upward, and spanwise inward directions, respectively. In the case of RW, any vertical differences along the

chordwise direction are caused by the angle of attack, and the wing maintains its original shape throughout the experiments. Compared with RW, the wings of EW1 and EW2 are both bent upward, and the bending intensity increases with elasticity. Particularly, significant deformations are observed at the wing tip, which are directly correlated with the position of the tip vortex.
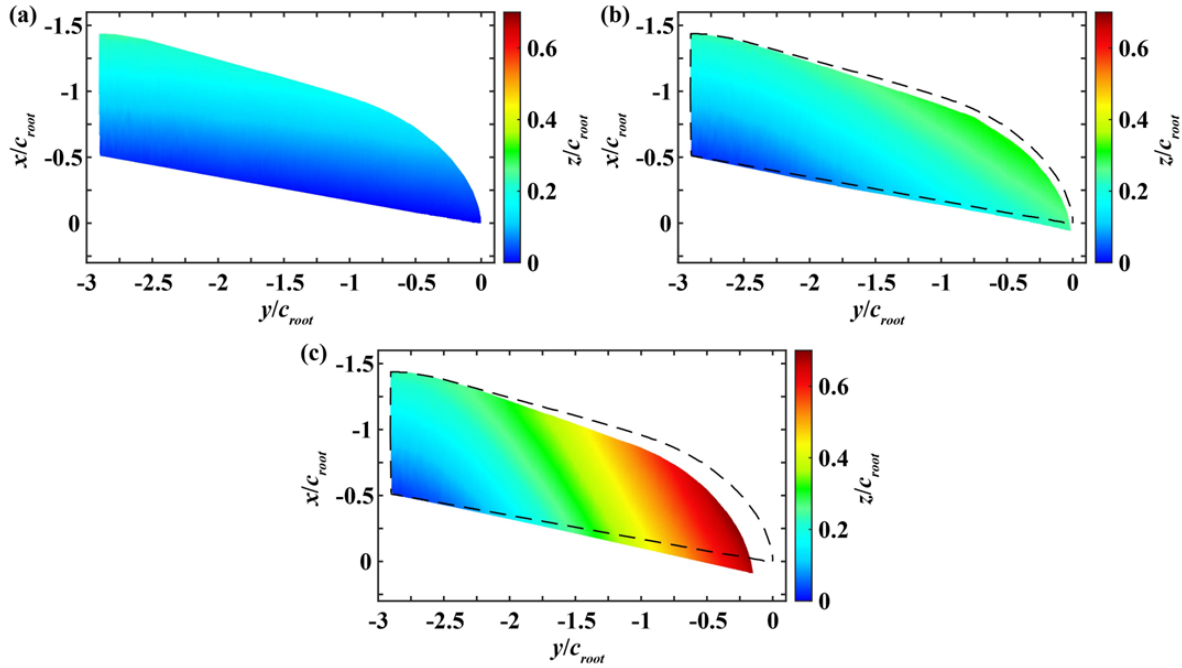

Figure. 2 Time-averaged wing shapes of (a) RW, (b) EW1, and (c) EW2 at *AoA* = 12°. The dashed lines in (b) and (c) show the outline of RW for a better presentation of the elastic wing deformation.

The wing tip positions at *AoA* = 6°, 12°, and 20° are summarized in Fig. 3, revealing that the tip moved not only vertically but also along the streamwise and spanwise directions. In Fig. 3(a), tip deformations along the streamwise direction are presented. The most downstream deformation of x/c_{root} = 0.22 is observed for EW2 at *AoA* = 20°. The farther downstream the tip position, the later the formation of the tip vortex is anticipated. Figures 3(b) and 3(c) illustrate the deformation projection in the cross-plane perpendicular to the freestream. The projection is more directly aligned with the aerodynamic characteristics described in the works of Guo et al. (2023). For EW2, the maximum deformations are observed at *AoA* = 20°, corresponding to the largest aerodynamic forces. For EW1, due to the lift increment at *AoA* = 12°, the maximum vertical deformation z/c_{root} of 0.24 is observed at this angle of attack rather than at the highest one. These deformations are not only the structural responses to the aerodynamic loads, but also a necessary consideration when examining the tip vortex in the following sections.
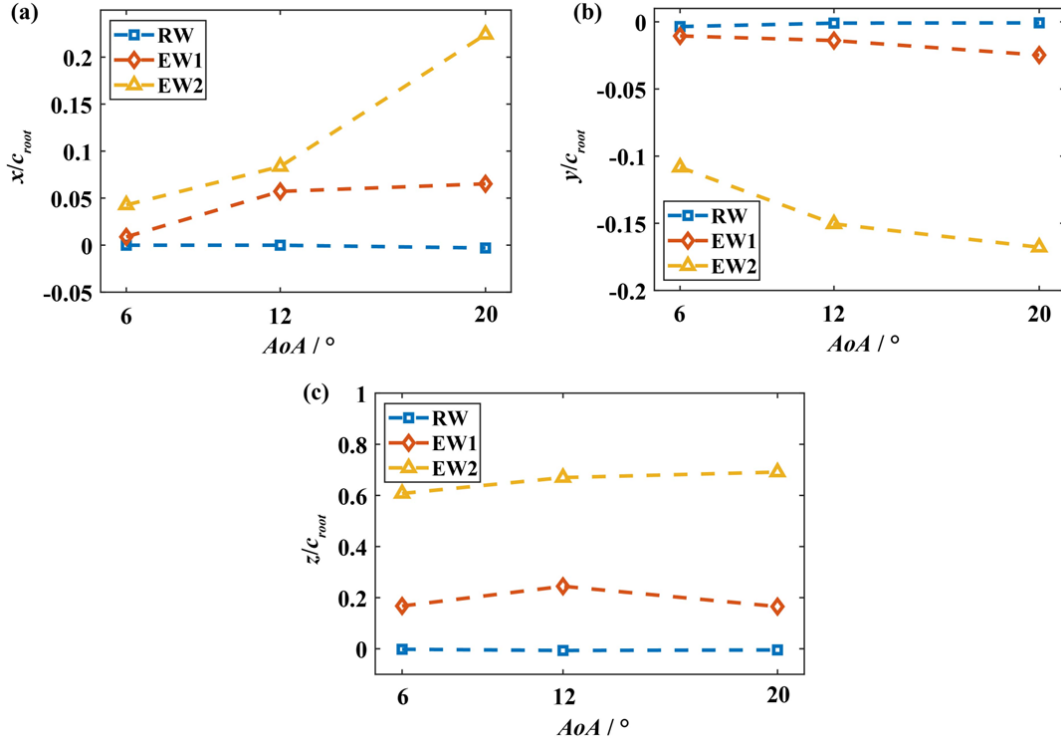
Figure. 3 Wing tip positions along (a) streamwise, (b) spanwise, and (c) vertical directions.

It was revealed that the elastic wings had two vibration modes, the torsional mode and the bending mode, which are also observed in the present experiments as shown in Fig. 4. The torsional mode is observed when the elastic wing is in the lift-enhancement regimes, and the maximum vibrations are observed near the leading- and trailing-edges. Bending modes are observed in the remaining experimental cases, where the dominant vibration is the vertical movement around the wing tip.

To precisely identify the torsional vibration intensity, Equation (1) is adopted to fit the instantaneous wing shapes.

$$z(x, y, t) = a(y, t) \times x + b(y, t) \tag{1}$$

where $a(y, t)$ represents the tangent of the angle of attack. By averaging $a(y, t)$ along spanwise y and subsequently subtracting its time-averaged value, the parameter, AoA', is obtained to represent the instantaneous fluctuations of the angle of attack. Similarly, the wing vertical bending is represented by the fluctuation of the wing's vertical position $\bar{z}'$, which is obtained by first spatially averaging z and then subtracting its time-averaged value.

Figures 4(c) and 4(d) show the scatter plots of the two modes based on AoA' and $\bar{z}'/c_{root}$. For the torsional vibration mode, it seems that the fluctuations of the angle of attack are almost independent of the vertical position. The peak-to-peak value of AoA' exceeds 4°, and that of $\bar{z}'$ is

about 1.5% of c_{root}. It is indicated that the torsional axis may also experience vertical vibration. For the bending mode, the peak-to-peak value of AoA' is no more than 1°, while the $\bar{z}'/c_{root}$ is varied over ±0.02.
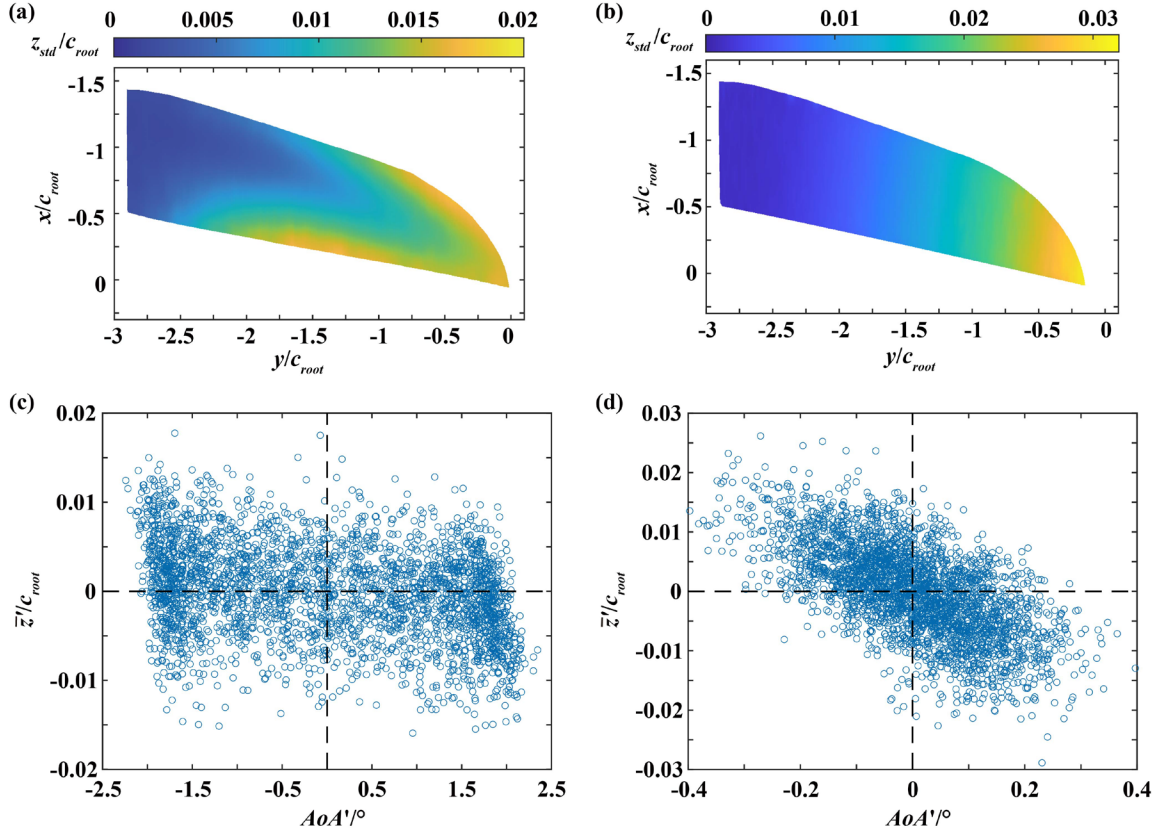

Figure. 4 (a) Torsional vibration mode of EW1 at AoA = 12°; (b) Bending vibration mode of EW2 at AoA = 12°; (c) Scatter plots of (c) torsional vibration mode and (d) bending vibration mode based on AoA' and $\bar{z}'/c_{root}$.

3.2 Tip vortex

The time-averaged vorticity at AoA = 6°, 12° and 20° is shown in Fig. 5. The vortex cores of the elastic wings have all moved spanwise inward and vertically upward, coinciding with the wing tip deformation. The maximum vortex movement is observed for EW2 with the vertical movement always over $0.5c_{root}$ compared to RW. For EW1, the strongest tip vortex is observed at AoA = 12° as a response to the lift increment regime. Comparing EW1 to RW, the core size, the distance from the vortex center to the position of peak tangential vorticity, increases significantly by nearly 50%.

Given that both the significantly strengthened vortex of EW1 and the shifted vortex of EW2 are observed at AoA = 12°, this angle of attack is taken as an example to illustrate the vortex downstream convection in the following.
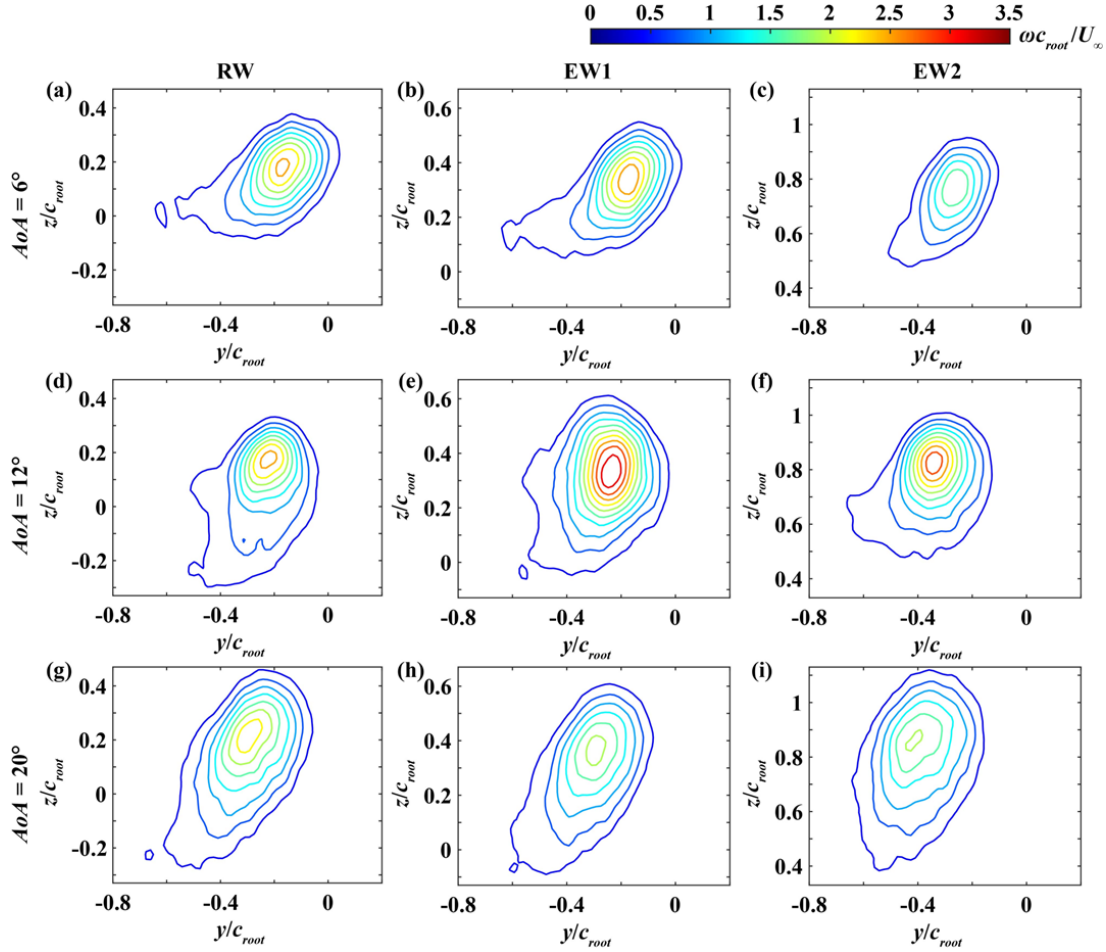
Figure. 5 Time-averaged vorticity $\omega/c_{root}U_\infty$ at x/c_{root} = 2. (a), (b), (c) AoA = 6°; (d), (e), (f) AoA = 12°; (g), (h), (i) AoA = 20°; (a), (d), (g) RW; (b), (e), (h) EW1; (c), (f), (i) EW2.

The vorticity contours at six cross-planes from x/c_{root} = 0.5 to 5 at AoA = 12° are displayed in Fig. 6. The time-averaged wing shapes are added for a better presentation of the relative position between the tip vortex and the wings. The tip vortex exhibits an asymmetric shape in the early wake, especially at x/c_{root} = 0.5. On the one hand, the wing bending contributes to this asymmetry. As the vortex wraps from the pressure side to the upper surface around the bent tip regions, it is elongated along the spanwise direction. On the other hand, the tip is moved downstream resulting in a shorter distance between the wings and the measured plane. The strong interaction between the tip vortex and the wake sheet also contributes to this asymmetry. When the tip vortex convects downstream, the vortex core disperses via viscous diffusion resulting in a relatively more circular shape with decreased vorticity.

Concerning the positions and strengths, the tip vortex remains the same regularity as discussed

before. The core of EW2 always remains the highest position around z/c_{root} = 0.8, and the EW1 obtains the strongest vortex core with a maximum core size.
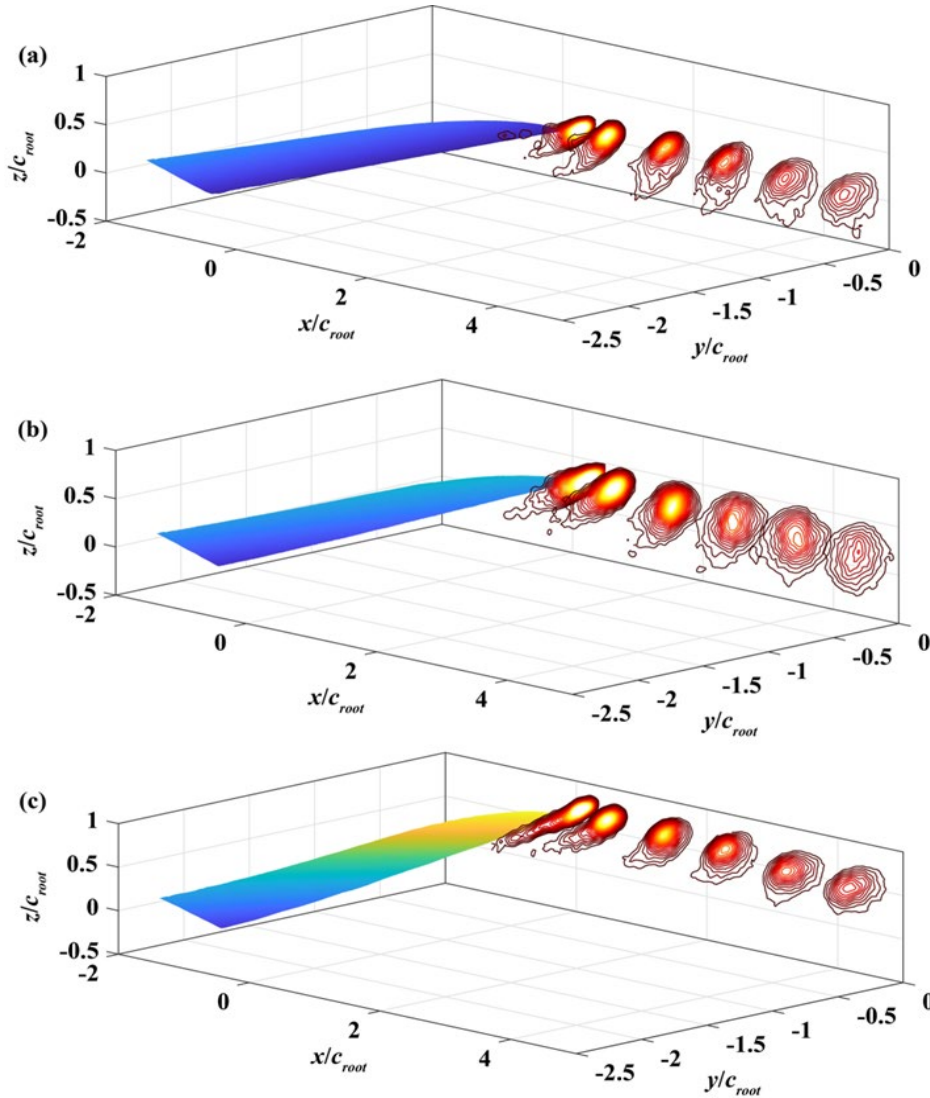

Figure. 6 Wing deformations and vorticity contours at six cross-planes of x/c_{root} = 0.5, 1, 2, 3, 4, 5 at AoA = 12° for (a) RW, (b) EW1, and (c) EW2.

4. Conclusion

To reveal the effects of elastic wing deformation on the tip vortex, two kinds of elastic wing and a rigid wing are investigated in low-speed wind tunnel experiments. The HADM method and SPIV are combined to capture the 3D deformations and 2D3C flow fields simultaneously. The main conclusions are as follows.

The wing exhibits greater bending with increased elasticity, causing the tip to move along the streamwise, vertically upward, and spanwise inward directions. These movements correlate with aerodynamic forces and influence the positions of the tip vortex. The highest tip vortex position is observed for EW2, which is higher than 0.5 times the length of wing root compared to RW. For EW1, the strongest vortex is obtained at *AoA* = 12° as a response to the lift increment regime.

In the early wakes, the tip vortex presents an asymmetric shape originating from the bent wing tips. At x/c_{root} = 0.5, the tip vortices of elastic wings are elongated along the spanwise direction. The more elastic the wing, the shorter the distance from the tip to the measured sections, resulting in a stronger interaction between the tip vortex and the wake sheet. This interaction could also contribute to the vortex asymmetry. As the tip vortex convects downstream, the vortex core disperses resulting in a relatively more circular shape and a decreased vorticity.

Acknowledgments

Nomenclature

a	Tangent of angle of attack [-]
AoA	Angle of attack [°]
AoA'	Fluctuation of spatially averaged angle of attack [°]
b	Intercept of linear fit [m]
c_{root}	Length of wing root [m]
E	Elastic modulus [GPa]
Re	Reynolds number [-]
t	Time [s]
U_∞	Free stream velocity [m/s]
x	Streamwise position [m]
y	Spanwise position [m]
z	Vertical position [m]
$\bar{z}'$	Fluctuation of spatially averaged vertical position [m]
ω	Vorticity [s^{-1}]

References

Anderson J. (1996) Aircraft Performances and Design. New York: McGraw Hill.

Bleischwitz, R., De Kat, R., & Ganapathisubramani, B. (2017). On the fluid-structure interaction of flexible membrane wings for MAVs in and out of ground-effect. *Journal of Fluids and Structures*, 70, 214-234.

Champagnat, F., Plyer, A., Le Besnerais, G., Leclaire, B., Davoust, S., & Le Sant, Y. (2011). Fast and accurate PIV computation using highly parallel iterative correlation maximization. *Experiments in Fluids*, 50(4), 1169-1182.

Guo, Q., Feng, S., & Wang, J. (2023). Effects of 3-D deformation of elastic wings on aerodynamic performance of an aircraft model. *Science China Technological Sciences*, 66(5), 1365-1377.

Guo, Q., He, X., Wang, Z. & Wang, J. (2021). Effects of wing flexibility on aerodynamic performance of an aircraft model. *Chinese Journal of Aeronautics*, 34(9), 133-142.

Guo, Q., & Wang, J. (2023). High-accuracy 3-D deformation measurement method with an improved structured-light principle. *Science China Technological Sciences*, 66(12), 3450-3461.

Gursul, I., Cleaver, D. J., & Wang, Z. (2014). Control of low Reynolds number flows by means of fluid–structure interactions. *Progress in Aerospace Sciences*, 64, 17-55.

He, X., & Wang, J. J. (2020). Fluid–structure interaction of a flexible membrane wing at a fixed angle of attack. *Physics of Fluids*, 32(12).

Lian, Y., Shyy, W., Viieru, D., & Zhang, B. (2003). Membrane wing aerodynamics for micro air vehicles. *Progress in Aerospace Sciences*, 39(6-7), 425-465.

Pan, C., Xue, D., Xu, Y., Wang, J., & Wei, R. (2015). Evaluating the accuracy performance of Lucas-Kanade algorithm in the circumstance of PIV application. *Science China Physics, Mechanics & Astronomy*, 58, 1-16.

Shyy, W., Ifju, P., & Viieru, D. (2005). Membrane wing-based micro air vehicles. *Applied Mechanics Reviews*, 58(4), 283-301.

Shyy, W., Klevebring, F., Nilsson, M., Sloan, J., Carroll, B., & Fuentes, C. (1999). Rigid and flexible low Reynolds number airfoils. *Journal of Aircraft*, 36(3), 523-529.

Song, A., Tian, X., Israeli, E., Galvao, R., Bishop, K., Swartz, S., & Breuer, K. (2008). Aeromechanics of membrane wings with implications for animal flight. *AIAA Journal*, 46(8), 2096-2106.

Takeda, M., & Mutoh, K. (1983). Fourier transform profilometry for the automatic measurement of 3-D object shapes. *Applied Optics*, 22(24), 3977-3982.

Tiomkin, S., & Raveh, D. E. (2021). A review of membrane-wing aeroelasticity. *Progress in Aerospace Sciences*, 126, 100738